Pressure evolution of quantum oscillations and electronic structure in ZrSiS

Tucker Beekmann,[1,*] Kyryl Shtefiienko,[1,*] Cole Phillips,[1] Rajesh Kumar Ulaganathan,[2] Raman Sankar,[3] David E. Graf,[4,5] and Keshav Shrestha[1,†]

[1]*Department of Chemistry and Physics, West Texas A&M University, Canyon, Texas 79016, USA*
[2]*Centre for Nanotechnology, Indian Institute of Technology, Roorkee 247667, India*
[3]*Institute of Physics, Academia Sinica, Nankang, Taipei 11529, Taiwan, People's Republic of China*
[4]*Department of Physics, Florida State University, Tallahassee, Florida 32306, USA*
[5]*National High Magnetic Field Laboratory, Tallahassee, Florida 32310, USA*

(Received 20 December 2025; accepted 30 March 2026; published 20 April 2026)

This work presents a systematic study of the pressure evolution of the electronic structure of ZrSiS using bulk magnetotransport measurements under hydrostatic pressure and first-principles calculations. Magnetoresistance measured at four pressure points (0.25, 0.47, 1.55, and 2.10 GPa) exhibits clear Shubnikov-de Haas oscillations characterized by five dominant frequencies, $F_\alpha = 17$, $F_\beta = 37$, $F_\gamma = 93$, $F_\delta = 138$, and $F_\epsilon = 242$ T, which remain nearly unchanged with increasing pressure. To probe the pressure evolution of the electronic states, the Berry phase (Φ_B) was extracted from Landau level fan diagram analyses. The extracted Φ_B values for the α and ϵ orbits show a systematic evolution with pressure, changing from values close to π at low pressure toward values approaching zero above ~0.47 GPa, suggesting a possible change in the electronic topology near this pressure. To further examine the evolution of the band topology, we calculated the topological invariants calculations. The results suggest nontrivial states at low pressures and a tendency toward trivial states at higher pressures, consistent with the experimentally observed evolution of the Berry phase. To further investigate the underlying electronic structure, first-principles calculations were performed up to 16 GPa. The calculated band structures reveal multiple Dirac crossings near the Fermi level derived primarily from Zr d and S p orbitals, which remain robust under pressure. Phonon dispersion calculations show no imaginary modes up to 16 GPa, confirming the dynamical stability of ZrSiS under hydrostatic compression. The combined experimental and theoretical results indicate that pressure modifies the electronic states without a pronounced reconstruction of the Fermi surface, highlighting the role of subtle changes in the electronic structure. These findings provide insight into pressure-driven electronic evolution in nodal-line semimetals and related quantum materials.

DOI: 10.1103/b4pt-rrpj

I. INTRODUCTION

Topological materials hosting Dirac-like electronic dispersions have attracted significant attention in recent years due to their symmetry-protected gapless states and unconventional electronic responses [1–7]. A prominent subclass is the topological nodal-line (TNL) semimetal, in which band crossings extend along one-dimensional manifolds—lines or closed loops—in momentum space, leading to an enhanced density of states and a variety of emergent quantum phenomena [8–11]. ZrSiS has emerged as a model TNL semimetal owing to its simple crystal structure, multiple Dirac cones in close proximity to the Fermi level, and an unusually large linear dispersion extending up to 2 eV [12,13]. High-quality single crystals can be readily grown using the chemical vapor transport method [14,15]. Combined with its air stability and the use of abundant, nontoxic elements, this makes ZrSiS particularly well suited for systematic experimental investigations. ZrSiS exhibits several remarkable properties, including extremely large and anisotropic magnetoresistance (MR) (~10^5%) [15–17] and negative longitudinal MR [15], signaling a chiral anomaly.

The electronic structure of ZrSiS has been extensively studied through quantum oscillation experiments [10,15,16,18–24], which established a complex, multisheet Fermi surface and revealed a nontrivial Berry phase associated with its Dirac fermions. High-field torque magnetometry measurements further demonstrated pronounced anisotropy of the Fermi surface [25]. These studies consistently confirm the topological nature of ZrSiS at ambient pressure.

Pressure provides a powerful means of tuning the lattice and electronic structure of quantum materials by directly modifying interatomic distances and orbital overlap [26–28]. It has been widely used to suppress competing orders, induce superconductivity, and control magnetic phases in correlated systems [29–34]. Pressure-induced topological phase transitions have also been reported in several quantum materials [35–40]. A few high-pressure and uniaxial strain studies on ZrSiS have demonstrated that this nodal-line semimetal is highly sensitive to lattice compression, revealing a range of pressure-induced phenomena [41–45]. These investigations have primarily focused on structural transitions using

*These authors contributed equally to this work.
†Contact author: kshrestha@wtamu.edu

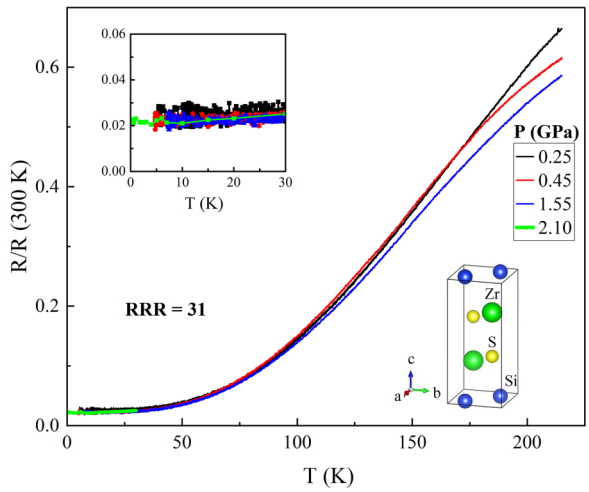

FIG. 1. Temperature dependence of the electrical resistance $R(T)$ of ZrSiS under various applied pressures. The data show metallic behavior with a residual resistivity ratio (RRR) of 31. Upper inset: Zoomed-in view of $R(T)$ at low temperatures. No superconductivity is observed up to 2.10 GPa and down to 0.3 K. Lower inset: Crystal structure of the ZrSiS unit cell.

high-pressure x-ray diffraction [41] and on magnetotransport measurements to probe possible topological transitions [43,44]. However, the reported critical pressures for the pressure-induced topological phase transition differ significantly, with values of 0.16–0.5 GPa [44] and 7.4 GPa [43]. This large discrepancy calls for a systematic re-examination of the low-pressure evolution of the electronic structure in ZrSiS using bulk-sensitive probes.

In this work, we combine magnetotransport measurements under hydrostatic pressure up to 2.10 GPa with first-principles calculations to investigate the pressure evolution of the electronic structure of ZrSiS. Well-defined Shubnikov-de Haas (SdH) oscillations are observed across the entire pressure range. Analysis of the Berry phase ($\Phi_\mathbf{B}$) extracted from Landau level fan diagrams reveals a pressure-induced evolution from a nontrivial value at low pressure toward a trivial value above ∼0.47 GPa, in close agreement with the lower-pressure regime reported previously [44]. Our electronic band structure calculations show multiple Dirac crossings near the Fermi level derived primarily from Zr d and S p orbitals, which remain robust up to 16 GPa. These results indicate that the pressure-driven electronic transition occurs without a pronounced reconstruction of the Fermi surface, suggesting that subtle changes in the underlying band topology, rather than changes in Fermi-surface geometry, play an important role.

II. EXPERIMENTAL AND COMPUTATIONAL DETAILS

High-quality single crystals of ZrSiS were synthesized using the chemical vapor transport (CVT) method. The details of the sample growth are provided in our recent article [25]. ZrSiS is a layered material with the tetragonal crystal structure (space group $P4/nmm$). The unit cell of ZrSiS is shown in the inset of Fig. 1. Electrical transport measurements under high pressure and magnetic fields up to 18 T were performed at the National High Magnetic Field Laboratory (NHMFL) in Tallahassee, FL. Hydrostatic pressure up to 2.10 GPa was generated using a piston-cylinder pressure cell. A shiny single crystal of ZrSiS was selected, and four electrical contacts were attached in a standard four-probe configuration for resistivity measurements. The sample was then mounted inside a piston-cylinder pressure cell for high-pressure experiments. Daphne 7474 oil served as the pressure-transmitting medium, and the applied pressure at low temperatures was calibrated by monitoring the fluorescence shift of a small ruby chip placed inside the cell. The crystal was oriented with the magnetic field directed parallel to the c axis. Magnetic fields up to 18 T were applied under pressure, and field sweeps were carried out at each fixed temperature at a rate of 0.3 T/min.

The electronic structure of ZrSiS was computed using the WIEN2k package [46], which employs the full-potential linearized augmented plane-wave (FLAPW) method within the DFT framework. The generalized gradient approximation (GGA) in the Perdew-Burke-Ernzerhof (PBE) form [47] was used to describe exchange-correlation effects. The self-consistent field (SCF) calculations were converged to 10^{-4} Ry, and the reduced muffin-tin radii (RMT) were set to 2.47, 2.22, and 2.24 Bohr for Zr, Si, and S, respectively. The $\mathbb{Z}_2$ topological invariants were evaluated using the FPLO (full-potential local-orbital) code [48,49]. Phonon calculations were carried out using the QUANTUM ESPRESSO package [50] with the PBEsol functional for exchange correlation. The plane-wave kinetic energy and charge-density cutoffs were 70 Ry and 280 Ry, respectively. Phonon dispersions were obtained using the finite-displacement method [51] on a $2 \times 2 \times 2$ supercell, as implemented in the PHONOPY package [52].

III. EXPERIMENTAL RESULTS

Figure 1 shows the temperature dependence of the electrical resistance R (T) at pressures up to 2.10 GPa. The sample displays typical metallic behavior, with a residual resistivity ratio, $RRR = R$ (300 K)$/R$ (5 K), of 31, indicating the high quality of the single crystal. This RRR value is comparable with the previous reports [12,45]. As shown in the upper inset, the resistance saturates at ∼20 μΩ at low temperatures; however, no signatures of superconductivity are observed down to 0.3 K. Previous bulk electrical transport studies [44] up to 1.7 GPa also reported no superconducting transition in this material. In contrast, superconductivity observed in point-contact spectroscopy [42] could be influenced by local interfacial doping or strain effects, whereas the present measurements under quasihydrostatic pressure probe the intrinsic bulk electronic response. Further point-contact measurements or complementary experimental probes may help clarify the nature and origin of possible superconducting phases in this material.

To investigate the electronic structures of this material, we applied *in situ* magnetic fields up to 18 T. As shown in Fig. 2, the material exhibits positive MR. The MR(%) is defined as $\frac{R(H)-R(0)}{R(0)} \times 100\%$, where $R(H)$ and $R(0)$ are the resistance values at field H and zero field, respectively. The MR reaches values as high as $1.3 \times 10^4\%$, as shown in

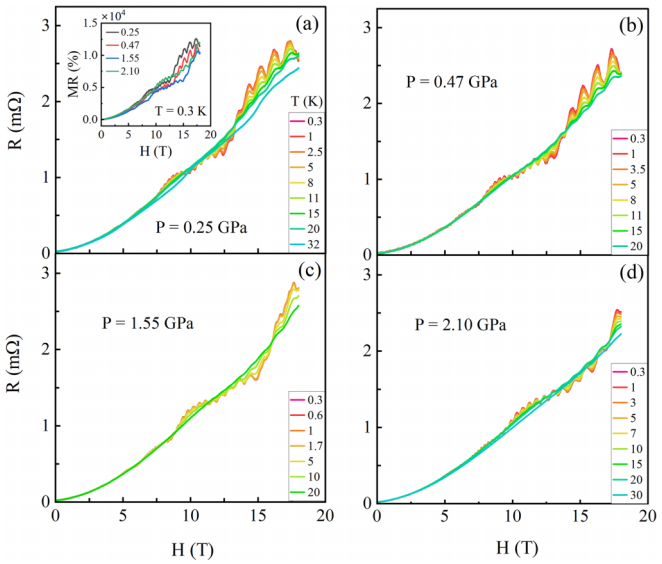

FIG. 2. Magnetoresistance (MR) of ZrSiS measured at (a) 0.25 GPa, (b) 0.47 GPa, (c) 1.55 GPa, and (d) 2.10 GPa. The MR remains positive across all pressures and displays clear Shubnikov-de Haas (SdH) oscillations. These oscillations gradually weaken with increasing temperature and disappear above 30 K. Inset of (a): MR values at different pressures at 0.3 K.

the inset of Fig. 2(a), and does not change significantly with pressure. Such large, nonsaturating MR in ZrSiS is consistent with previous reports [15–18], and the values observed here are comparable. In addition to this large MR, clear SdH oscillations are observed. The oscillations start above 5 T and become more prominent at higher fields. Oscillations are observed at all measured pressures (0.25, 0.47, 1.55, and 2.10 GPa). Their amplitudes gradually decrease with increasing temperature and disappear above 30 K. As seen in Fig. 2, the oscillations are periodic, well defined, and appear to contain more than one frequency.

The frequency of the SdH oscillations is determined by taking the Fourier transform. For this, the MR data are first fitted with a smooth polynomial background, which is then subtracted to extract the oscillatory component. We then carried out the fast Fourier transform (FFT) to extract the frequency signals. The FFT spectra for each of the pressure points are shown in Fig. 3. The FFT spectrum is rich and possesses five distinct peaks. At ambient pressure [Fig. 3(a)], there are peaks at $F_\alpha = 17$, $F_\beta = 37$, $F_\gamma = 93$, $F_\delta = 138$, and $F_\epsilon = 242$ T. The frequency spectrum shown in Fig. 3 is comparable to those reported from torque measurements [10,25] and magnetothermoelectric studies [23]. In contrast, previous magnetotransport studies on ZrSiS [15,16,22] resolved only two oscillation frequencies near 17 T and 242 T. In the present work, we resolved five distinct SdH frequencies, which we

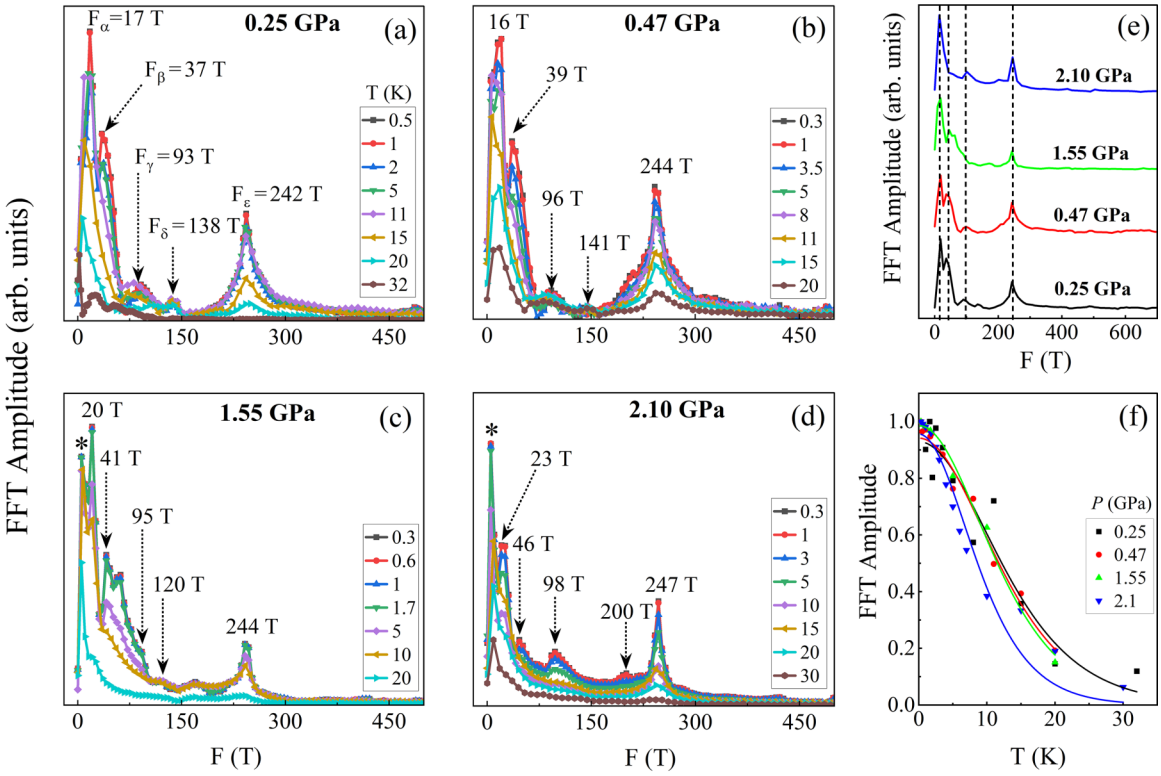

FIG. 3. Frequency spectra of the quantum oscillations of ZrSiS at (a) 0.25 GPa, (b) 0.47 GPa, (c) 1.55 GPa, and (d) 2.10 GPa. Five prominent frequencies—17, 37, 93, 138, and 242 T—are visible at 0.25 GPa. With increasing pressure, these peaks exhibit a slight shift in position. The small feature near 7 T, marked by a star, originates from imperfect background subtraction. (e) Comparison of the FFT spectra at 0.3 K under 0.25, 0.47, 1.55, and 2.10 GPa. The graphs are shifted vertically for better visibility. The major peaks, marked by dashed lines, remain unchanged with pressure. (f) Temperature dependence of the FFT amplitude for the ∼ 245 T frequency at each pressure. The solid curves represent the best fits to the data using the Lifshitz-Kosevich formula (1).

TABLE I. SdH frequencies (F, in T) and effective mass m^* of ZrSiS under different pressures. The ambient-pressure data are taken from our previous report [25].

P (GPa)	F_α	F_β	F_γ	F_δ	F_ϵ	m^*/m_0
0	17	33	100		242	0.052
0.25	17	37	93	138	242	0.205
0.47	16	39	96	141	244	0.215
1.55	20	41	95	120	244	0.228
2.10	23	46	98	200	247	0.296

attribute to the high sensitivity and precision of the experimental setup at the SCM2 facility of the NHMFL.

At higher pressure points too, the frequency peaks are well resolved, Figs. 3(b)–3(d). At 1.55 GPa, the FFT spectrum exhibits a broadened response in the frequency range corresponding to the F_γ and F_δ branches, appearing as a shoulderlike feature and a shallow hump rather than two well-separated peaks. While these frequencies are clearly resolved at lower pressures, their separation becomes less distinct at 1.55 GPa due to peak broadening and partial overlap. The identification of F_γ and F_δ at this pressure is based on the systematic tracking of the FFT peak positions as a function of pressure, with these features occurring at frequencies consistent with the continuous evolution of F_γ and F_δ at neighboring pressure points.

There appears to be a slight change in peak position; however, it does not look very significant. We plotted FFT spectrum at the base temperature ($T = 0.3$ K) at different pressure points [Fig. 3(e)]. As indicated by the vertical lines in the graph, there is negligible change in the frequency value with pressure. Such behavior of nearly unchanged frequency peak with pressure has recently been observed in recent magnetotransport studies [43]. According to Onsager's relation [1,53,54], the quantum oscillation frequency F is directly proportional to the extremal cross-sectional area of the Fermi surface A_F as $F = \frac{\hbar}{2\pi e} A_F$, where $\hbar$ and e are the reduced Planck's constant and the charge of an electron, respectively. Therefore, nearly unchanged values of frequency peaks in Fig. 4(c) and Table I indicate that the Fermi surface, that is, the electronic structure of ZrSiS, remains nearly unchanged with the pressure up to 2.10 GPa.

As seen in Fig. 2, the amplitude of the oscillations decrease at higher temperatures, this feature is also reflected in the FFT spectrum shown in Fig. 3. The temperature dependence of quantum oscillations can be described by the Lifshitz-Kosevich (LK) formula [55,56]. According to the LK theory, the temperature and magnetic field dependence of quantum oscillations is given by

$$\Delta R(T,H) \propto e^{-\lambda_D(H)} \frac{\lambda(T/H)}{\sinh[\lambda(T/H)]}, \tag{1}$$

with $\lambda_D(H) = \frac{2\pi^2 K_B}{\hbar e} m^* \frac{T_D}{H}$ and $\lambda(T/H) = \frac{2\pi^2 K_B}{\hbar e} m^* \frac{T}{H}$. Here, T_D, K_B, and m^* represent the Dingle temperature, Boltzmann's constant, and effective mass of the charge carriers, respectively. The first term is the Dingle factor, which describes the attenuation of the oscillations with decreasing field H. The second term explains the weakening of the oscillations at higher temperatures. By fitting the temperature dependence of

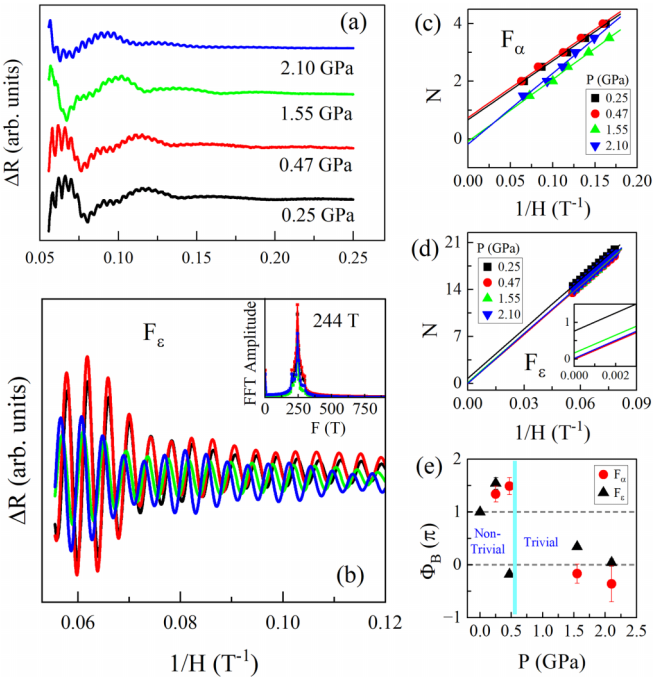

FIG. 4. (a) Background-subtracted resistance data for ZrSiS at different pressures. Shubnikov-de Haas (SdH) oscillations are clearly visible with low and high frequency signals. (b) SdH oscillations corresponding to the frequency F_ϵ obtained after using the band-pass filter of (200–300) T. The filtered oscillations has a single frequency signal F_ϵ, as shown in the inset. Landau-level (LL) fan diagram for (c) F_α and (d) F_ϵ, obtained by assigning integer indices N to the maxima and $N + 1/2$ to the minima of the quantum oscillations. The solid lines show the linear extrapolation of the data as $1/H \to 0$. The lower inset in (d) is the zoomed-in view of the LL plot highlighting the intercepts. (e) The pressure dependence of the Berry phase $\Phi_\mathbf{B}$ for the α and ϵ orbits. $\Phi_\mathbf{B}$ for both orbits changes from $\sim\pi$ to 0 above 0.47 GPa, indicating the topological phase transition. The ambient-pressure value of $\Phi_\mathbf{B}$ is adopted from Ref. [16].

FFT data with the LK formula, we can estimate the effective mass of the charge carriers.

Figure 3(f) shows the amplitude versus temperature plot for F_ϵ at different pressure points. Here, we selected F_ϵ as it is the prominent peak and observed at wide temperature range up to 30 K. In the graph, the scattered points are the raw data and the dotted curves are the best fits using the LK formula (1). From the analyses, we estimated $m^* = 0.205m_o$, $0.215m_o$, $0.228m_o$, and $0.296m_o$, where m_o is the rest mass of electron, at 0.25, 0.47, 1.55, and 2.10 GPa, respectively. There is slight increase in m^* at higher pressure. The variation of the frequency peaks along with m^* with pressure is listed in Table I. We have included the data at 0 GPa from our previous torque measurements [25]. As seen in the table, there are small variation of frequency values with increasing pressure.

To estimate $\Phi_\mathbf{B}$ and thereby probe the topological nature of ZrSiS, we employ the Landau level (LL) fan diagram analysis. For topologically trivial systems, $\Phi_\mathbf{B} = 0$, whereas for topologically nontrivial systems, $\Phi_\mathbf{B} = \pi$ [1,57,58]. As shown in Fig. 3, five dominant oscillation frequencies are observed. Among them, the F_α and F_ϵ peaks are the most prominent, are well separated from the other frequencies, and are present at

all measured pressures. Therefore, we use the SdH oscillations associated with these two frequencies to extract $\Phi_{\mathbf{B}}$. Although F_δ is also relatively well separated from the other peaks, its amplitude is much smaller, and thus it was not selected for the Berry phase analysis.

Figure 4(a) shows the background-subtracted resistance data at different pressure points. As expected, multiple oscillation periods are observed, indicating the presence of multiple frequencies. To isolate the oscillations corresponding to F_α and F_ϵ, we employed the band-pass filter option in OriginLab. Figure 4(b) shows the filtered SdH oscillations at different pressures obtained using a band-pass filter of 200–300 T. The presence of a single dominant frequency near 244 T in the inset confirms that the band-pass filtering successfully isolates the F_ϵ component. The same procedure was applied to select the oscillations corresponding to F_α.

Following Ando and previous studies [1,7,54,59], integer and half-integer Landau level indices are assigned to the minima and maxima of the conductivity, respectively, when constructing the Landau level fan diagram. Since the Hall resistivity is negligible compared to the longitudinal resistivity, the conductivity can be approximated as inversely proportional to the resistivity. Therefore, the minima and maxima of the resistivity are assigned integer N and half-integer $N + 1/2$ indices, respectively, for the Landau level fan plot. The resulting LL fan diagrams for F_α and F_ϵ are shown in Figs. 4(c) and 4(d), respectively. To extract the Berry phase $\Phi_{\mathbf{B}}$, a linear extrapolation was performed in the limit $1/H \to 0$. For the F_ϵ orbit, this analysis yields intercepts of $N_0 = 0.77$, -0.09, 0.17, and 0.02 at pressures of 0.25 GPa, 0.47 GPa, 1.55 GPa, and 2.10 GPa, respectively. These intercepts correspond to Berry phase values of $\Phi_{\mathbf{B}} = (1.54 \pm 0.11)\pi$, $(-0.18 \pm 0.06)\pi$, $(0.34 \pm 0.03)\pi$, and $(0.04 \pm 0.07)\pi$ at the respective pressures.

A similar procedure was followed to determine $\Phi_{\mathbf{B}}$ for the F_α orbit. The pressure dependence of $\Phi_{\mathbf{B}}$ for both the α and ϵ orbits is shown in Fig. 4(e). For comparison, the ambient-pressure value of $\Phi_{\mathbf{B}}$ is taken from Ref. [16]. As evident from the figure, $\Phi_{\mathbf{B}}$ evolves from a value close to π to zero above 0.47 GPa, indicating a pressure-induced topological phase transition in this compound. This critical pressure is in good agreement with the previously reported range of 0.16–0.5 GPa by VanGennep *et al.* [44].

IV. DFT CALCULATIONS

To gain further insight into the electronic structure of ZrSiS, we performed DFT calculations of the electronic band structure and Fermi surface. Figure 5 shows the orbital-resolved electronic band structure of ZrSiS along the high-symmetry k path in the Brillouin zone, as indicated in the inset. Multiple Dirac crossings are observed at or in close proximity to the Fermi level, as highlighted by the dotted circles. The linear band dispersion extends over a wide energy range of nearly 2 eV, most notably for the Dirac cone along the A–Z direction. Importantly, the electronic states near the Fermi level and the associated Dirac crossings are primarily derived from Zr d and S p orbitals. The calculated band structure is in good agreement with previous DFT studies on ZrSiS [12,13].

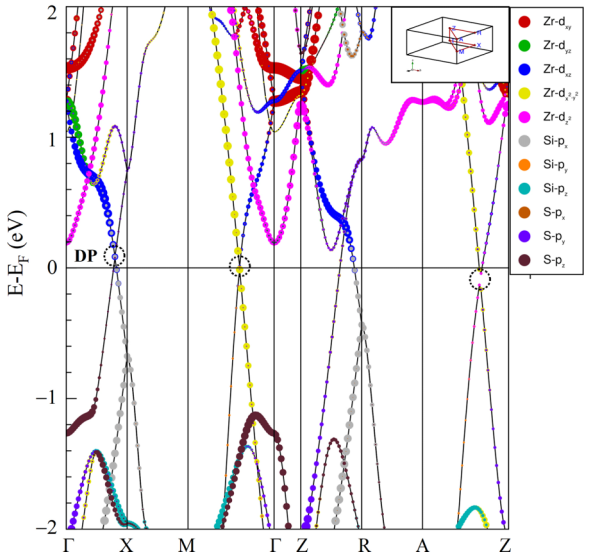

FIG. 5. Orbital-resolved electronic band structure of ZrSiS. Dirac points (DPs) near the Fermi level are highlighted by dotted circles and are primarily derived from Zr d and S p orbitals. Inset: high-symmetry k path.

Upon application of pressure up to 2.10 GPa [Fig. 6(a)], the electronic bands largely overlap, indicating that there is little to no change in the electronic structure within this pressure range. This behavior is consistent with our experimental observation of nearly unchanged frequency peaks under pressure (Fig. 3). To further examine the effect of pressure, we increased the pressure up to 16 GPa, as shown in Fig. 6(b). As seen in the figure, the positions of the Dirac points with

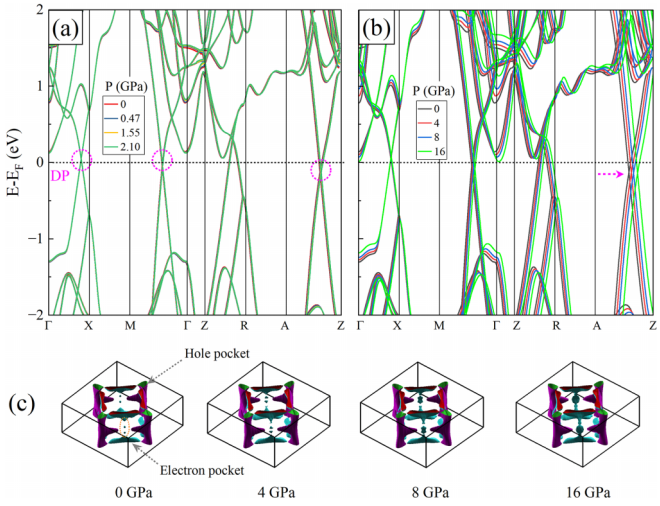

FIG. 6. Electronic band structure of ZrSiS at various pressures. Dirac points (DPs) are highlighted by dotted circles. (a) Up to 2.10 GPa, the band structure shows no noticeable change. (b) At 0, 4, 8, and 16 GPa, the DPs shift slightly to the right, while their energy positions remain unchanged, as indicated by the dashed arrow. (c) Fermi surface of ZrSiS at 0, 4, 8, and 16 GPa. The electron pocket shows a gradual expansion and reconnection between its upper and lower sections, while the hole pocket remains nearly unchanged, as shown by the dashed area.

respect to the Fermi level remain nearly unchanged. In particular, the Dirac point along the $A-Z$ direction shifts toward higher momentum; however, its energy relative to the Fermi level remains the same. One possible origin of this shift in the Dirac-like dispersion along the $A-Z$ direction with increasing pressure is the enhancement of interlayer hopping. As hydrostatic pressure reduces the interlayer spacing in ZrSiS, the out-of-plane electronic coupling becomes stronger, leading to increased k_z dispersion of the relevant bands. This modification of the out-of-plane hopping amplitudes can shift the momentum position of the Dirac crossing along the $A-Z$ path, producing the rightward displacement observed in the calculated band structure. Although other pressure-induced effects—such as changes in orbital hybridization or subtle structural distortions—may also contribute, enhanced interlayer coupling could be the possible reasons for the observed trend.

Two bands cross the Fermi level and they are responsible for the Fermi surface of ZrSiS. Figure 6(c) illustrate the Fermi surface at 0, 4, 8, and 16 GPa. The Fermi surface at 0 GPa are consistent with previous reports [16,19]. As seen in the graph, the Fermi surface due to the hole pocket remain nearly unchanged. While the Fermi surface due to the electron pocket, especially the sections connecting the upper and lower parts, initially are disconnected at 0 GPa. The middle sheetlike section grows gradually and connects them at 16 GPa.

It is important to note that although our DFT calculations indicate noticeable modifications of the Fermi surface only at much higher pressures (above 8 GPa), the experimental quantum oscillation frequencies remain nearly unchanged up to 2.10 GPa. Importantly, the Berry phase extracted from the α and ϵ orbits exhibits a clear evolution from a nontrivial value at low pressure toward a trivial value above 0.47 GPa. This indicates that the pressure-induced transition observed experimentally is primarily associated with a change in band topology rather than a reconstruction of the Fermi surface area. Such a topological transition can occur without a pronounced change in extremal orbit size or quantum oscillation frequency, consistent with the nearly pressure-independent SdH frequencies observed in our measurements.

It is worth noting that the Berry phase extracted from Landau fan diagrams (Fig. 4) may be influenced by several factors, including overlapping oscillation frequencies and possible pressure-induced changes in the band curvature or chemical potential. Therefore, the Berry phase analysis alone may not uniquely determine the topological nature of the system. To further examine the evolution of the band topology under pressure, we calculated the $\mathbb{Z}_2$ topological invariants using the FPLO code, following the methodology reported in our previous studies [60,61]. The topological nature of a material can be characterized by four Z_2 invariants $(\nu_0;\nu_1\nu_2\nu_3)$, which distinguish strong and weak topological phases. If $\nu_0 = 1$ and the other indices $(\nu_1\nu_2\nu_3)$ are equal to zero, the material is classified as a strong topological material. If $\nu_0 = 0$ and any of the indices $(\nu_1\nu_2\nu_3)$ is equal to one, the material is considered a weak topological material. The calculated invariants for ZrSiS at different pressure points are summarized in Table II. As shown in Table II, the results suggest nontrivial states at 0 and 1 GPa, while the system becomes trivial at 1.5 and 4 GPa, indicating a possible pressure-induced change in the topological state.

TABLE II. Pressure dependence of the $\mathbb{Z}_2$ topological invariants and the corresponding electronic phase.

Pressure (GPa)	$\nu_0;(\nu_1\nu_2\nu_3)$	Comments
0	1; (000)	Strong topological state
1	1; (000)	Strong topological state
1.5	0; (000)	Trivial state
4	0; (000)	Trivial state

To check the dynamical stability of ZrSiS under external pressure, we computed the phonon dispersion relations along high-symmetry directions of the Brillouin zone together with the corresponding atom-resolved phonon density of states (DOS) at pressures of 0, 4, 8, and 16 GPa, as shown in Figs. 7(a)–7(d). At ambient pressure [Fig. 7(a)], our phonon spectrum is consistent with the previously reported spectrum [13,41,62,63]. The absence of imaginary frequencies throughout the entire Brillouin zone, confirming the intrinsic dynamical stability of the tetragonal ZrSiS structure. Upon application of pressure up to 16 GPa [Figs. 7(b)–7(d)], no soft modes or imaginary frequencies emerge, demonstrating that the crystal structure remains dynamically stable under compression up to 16 GPa.

With the increase of pressure, there is a clear pressure-induced hardening of phonon modes. Both acoustic and optical branches exhibit systematic upward shifts in frequency over the full Brillouin zone, reflecting enhanced interatomic force constants and bond stiffening under compression. The hardening is particularly pronounced for the high-frequency optical modes, which are primarily associated with vibrations of the lighter S and Si atoms, while the lower-frequency modes are dominated by Zr vibrations, as evidenced by the atom-projected phonon DOS in Figs. 7(b)–7(d). The phonon DOS further supports these trends.

With increasing pressure, the DOS spectral weight progressively shifts toward higher frequencies, accompanied by a broadening of the optical phonon features. This behavior indicates an overall increase in lattice rigidity and reduced anharmonicity under compression. The absence of phonon softening or mode crossing suggests that no pressure-induced structural phase transition occurs within the studied pressure range. The observed pressure-driven phonon hardening implies a concomitant increase in elastic stiffness and may significantly influence thermodynamic and thermal transport properties, such as the Debye temperature and lattice thermal conductivity, under high-pressure conditions. These results establish the robust dynamical stability of ZrSiS and provide a solid foundation for further investigations of its pressure-dependent vibrational and thermal properties.

Quantum oscillation measurements under high pressure are experimentally challenging and often exhibit reduced signal-to-noise ratios due to the limited sample volume and background contributions from the pressure cell and pressure medium. To enhance the signal-to-noise ratio, the measurements were carried out down to 0.3 K using a ^{3}He system. While the oscillations corresponding to the low frequency F_α are not sharply defined and exhibit only a few maxima

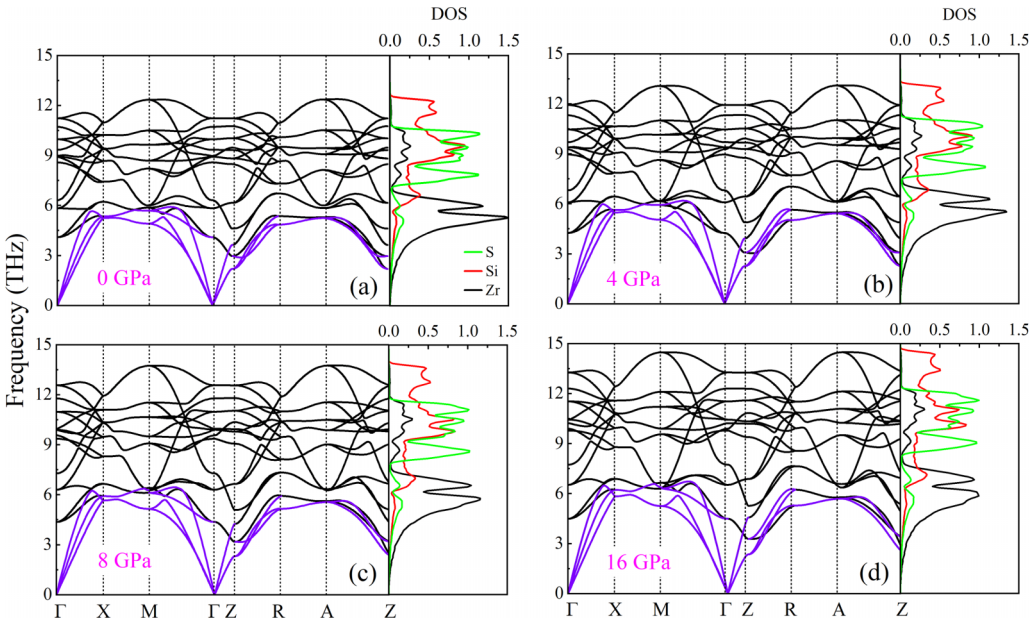

FIG. 7. Phonon dispersion relations and phonon density of states (DOS) of ZrSiS under hydrostatic pressures of (a) 0 GPa, (b) 4 GPa, (c) 8 GPa, and (d) 16 GPa. The absence of imaginary modes across all pressures indicates that ZrSiS remains dynamically stable throughout this range.

and minima [Fig. 4(a)], the oscillations associated with F_ϵ are well defined and display multiple maxima and minima. The frequency F_ϵ further follows the expected temperature dependence described by the LK formalism [Fig. 3(f)] at different pressures. These observations support their assignment as quantum oscillation features. However, due to their comparatively small amplitudes, particularly for F_α, a minor contribution from experimental noise cannot be completely excluded, and therefore the parameters extracted from these weaker features should be interpreted with some caution.

V. SUMMARY

We have investigated the pressure evolution of the electronic structure in the topological nodal-line semimetal ZrSiS using bulk magnetotransport measurements and first-principles calculations. Magnetoresistance measurements performed in magnetic fields up to 18 T reveal clear Shubnikov-de Haas (SdH) oscillations, from which five fundamental frequencies, $F_\alpha = 17$, $F_\beta = 37$, $F_\gamma = 93$, $F_\delta = 138$, and $F_\epsilon = 242$ T, are resolved. By analyzing the Landau level fan diagrams, we extracted the Berry phase Φ_B for the F_α and F_ϵ orbits at different pressures. The extracted phase shows a systematic evolution with pressure, suggesting a possible change in the topological character of the electronic states above ∼0.47 GPa. This pressure range falls within the low-pressure regime of 0.16–0.5 GPa reported by VanGennep *et al.* [44]. The apparent discrepancy with higher critical pressures reported in other studies (e.g., ∼7.4 GPa by Gu *et al.* [43]) may arise from differences in experimental probes and the criteria used to identify topology-related changes.

First-principles calculations reveal multiple Dirac crossings near or at the Fermi level, predominantly derived from Zr d and S p orbitals. Up to 2.10 GPa, the overall electronic band structure and the locations of the Dirac points remain nearly unchanged. At higher pressures, however, the Dirac crossing along the $A-Z$ direction exhibits a shift in momentum, suggesting enhanced interlayer coupling under compression. Complementary phonon dispersion calculations show no imaginary modes up to 16 GPa, confirming the dynamical stability of ZrSiS under hydrostatic pressure.

As shown in Fig. 3(e) and summarized in Table I, the SdH frequencies F_α and F_ϵ remain nearly pressure independent up to 2.10 GPa, indicating the absence of a significant Fermi surface reconstruction. Consistently, DFT calculations show no substantial changes in the electronic band structure, including the Dirac points [Fig. 6(a)], over this pressure range. While the Berry phase analysis indicates a pressure-induced evolution of the phase offset, such changes may also be influenced by factors such as chemical potential shifts or band curvature effects. To further examine the evolution of the band topology under pressure, we computed the $\mathbb{Z}_2$ topological invariants. The calculated invariants suggest nontrivial states at low pressures and a tendency toward trivial states at higher pressures, which is consistent with the experimentally observed evolution of the Berry phase.

Taken together, our results demonstrate that pressure provides an effective tuning parameter for modifying the electronic structure of ZrSiS. The combined experimental observations and first-principles calculations suggest a possible pressure-induced change in the topological character of the electronic states at low pressures. These findings highlight the sensitivity of nodal-line semimetals to external pressure and motivate further experimental and theoretical studies to clarify the microscopic origin of the observed behavior.

ACKNOWLEDGMENTS

This work was supported in part by the U.S. Department of Energy, Office of Science, Office of Workforce

Development for Teachers and Scientists (WDTS) under the Visiting Faculty Program (VFP) at Los Alamos National Laboratory, administered by the Oak Ridge Institute for Science and Education. The work at West Texas A&M University (WTAMU) is supported by the Killgore Undergraduate and Graduate Student Research Grants, the Welch Foundation (Grant No. AE-0025), and the National Science Foundation (Award No. 2336011). The computations were performed on the WTAMU HPC cluster, which was funded by the National Science Foundation (NSF CC* GROWTH 2018841). A portion of this work was performed at the National High Magnetic Field Laboratory, which is supported by National Science Foundation Cooperative Agreement No. DMR-2128556 and the State of Florida. R.S. acknowledges the financial support provided by the Ministry of Science and Technology in Taiwan under Projects No. NSTC-114-2124-M-001-009 and No. NSTC-113-2112-M-001-045-MY3, and Academia Sinica for the budget of AS-iMATE-114-12. R.K.U. would like to acknowledge the Prime Minister Early Career Research Grant (PM-ECRG) from the Anusandhan National Research Foundation (ANRF), India, under Grant Code No. ANR-2670-NTC-CNA/25 and the IITR for the Faculty Initiation Grant No. (FIG-101068).

DATA AVAILABILITY

The data that support the findings of this article are not publicly available. The data are available from the authors upon reasonable request.

[1] Y. Ando, Topological insulator materials, J. Phys. Soc. Jpn. **82**, 102001 (2013).

[2] X.-L. Qi and S.-C. Zhang, Topological insulators and superconductors, Rev. Mod. Phys. **83**, 1057 (2011).

[3] K. Shrestha, R. Chapai, B. K. Pokharel, D. Miertschin, T. Nguyen, X. Zhou, D. Y. Chung, M. G. Kanatzidis, J. F. Mitchell, U. Welp, D. Popovic, D. E. Graf, B. Lorenz, and W. K. Kwok, Nontrivial Fermi surface topology of the kagome superconductor CsV_3Sb_5 probed by de Haas–van Alphen oscillations, Phys. Rev. B **105**, 024508 (2022).

[4] M. Z. Hasan and C. L. Kane, *Colloquium*: topological insulators, Rev. Mod. Phys. **82**, 3045 (2010).

[5] Y. Xia, D. Qian, D. Hsieh, L. Wray, A. Pal, H. Lin, A. Bansil, D. Grauer, Y. S. Hor, R. J. Cava, *et al.*, Observation of a large-gap topological-insulator class with a single Dirac cone on the surface, Nat. Phys. **5**, 398 (2009).

[6] Y. Ando and L. Fu, Topological crystalline insulators and topological superconductors: From concepts to materials, Annu. Rev. Condens. Matter Phys. **6**, 361 (2015).

[7] K. Shrestha, V. Marinova, B. Lorenz, and P. C. Chu, Shubnikov–de Haas oscillations from topological surface states of metallic $Bi_2Se_{2.1}Te_{0.9}$, Phys. Rev. B **90**, 241111(R) (2014).

[8] G. Bian, T.-R. Chang, R. Sankar, S.-Y. Xu, H. Zheng, T. Neupert, C.-K. Chiu, S.-M. Huang, G. Chang, I. Belopolski, *et al.*, Topological nodal-line fermions in spin-orbit metal $PbTaSe_2$, Nat. Commun. **7**, 10556 (2016).

[9] K. Yokoi, H. Murakawa, H. Sakai, and N. Hanasaki, Anomalous Nernst effect in the nonmagnetic nodal-line semimetal $PbTaSe_2$, Phys. Rev. B **106**, 115118 (2022).

[10] J. Hu, Z. Tang, J. Liu, Y. Zhu, J. Wei, and Z. Mao, Nearly massless Dirac fermions and strong Zeeman splitting in the nodal-line semimetal ZrSiS probed by de Haas–van Alphen quantum oscillations, Phys. Rev. B **96**, 045127 (2017).

[11] B. Gudac, M. Bosnar, F. Orbanić, T. Ivšić, I. Kokanović, and M. Novak, In-plane Fermi surface mapping of ZrSiS and HfSiS by de Haas-van Alphen oscillations, SciPost Physics Proceedings 019 (2023).

[12] C.-C. Su, C.-S. Li, T.-C. Wang, S.-Y. Guan, R. Sankar, F. Chou, C.-S. Chang, W.-L. Lee, G.-Y. Guo, and T.-M. Chuang, Surface termination dependent quasiparticle scattering interference and magneto-transport study on ZrSiS, New J. Phys. **20**, 103025 (2018).

[13] A. N. Rudenko and S. Yuan, Electron-phonon interaction and zero-field charge carrier transport in the nodal-line semimetal ZrSiS, Phys. Rev. B **101**, 115127 (2020).

[14] R. Sankar, G. Peramaiyan, I. P. Muthuselvam, C. J. Butler, K. Dimitri, M. Neupane, G. N. Rao, M.-T. Lin, and F. Chou, Crystal growth of Dirac semimetal ZrSiS with high magnetoresistance and mobility, Sci. Rep. **7**, 40603 (2017).

[15] R. Singha, A. K. Pariari, B. Satpati, and P. Mandal, Large nonsaturating magnetoresistance and signature of nondegenerate Dirac nodes in ZrSiS, Proc. Natl. Acad. Sci. USA **114**, 2468 (2017).

[16] M. N. Ali, L. M. Schoop, C. Garg, J. M. Lippmann, E. Lara, B. Lotsch, and S. S. Parkin, Butterfly magnetoresistance, quasi-2D Dirac Fermi surface and topological phase transition in ZrSiS, Sci. Adv. **2**, e1601742 (2016).

[17] Y.-Y. Lv, B.-B. Zhang, X. Li, S.-H. Yao, Y. Chen, J. Zhou, S.-T. Zhang, M.-H. Lu, and Y.-F. Chen, Extremely large and significantly anisotropic magnetoresistance in ZrSiS single crystals, Appl. Phys. Lett. **108**, 244101 (2016).

[18] X. Wang, X. Pan, M. Gao, J. Yu, J. Jiang, J. Zhang, H. Zuo, M. Zhang, Z. Wei, W. Niu, *et al.*, Evidence of both surface and bulk Dirac bands and anisotropic nonsaturating magnetoresistance in ZrSiS, Adv. Electron. Mater. **2**, 1600228 (2016).

[19] C. S. A. Müller, T. Khouri, M. R. nan Delft, S. Pezzini, Y.-T. Hsu, J. Ayres, M. Breitkreiz, L. Schoop, A. Carrington, N. E. Hussey, and S. Wiedmann, Determination of the Fermi surface and field-induced quasiparticle tunneling around the Dirac nodal loop in ZrSiS, Phys. Rev. Res. **2**, 023217 (2020).

[20] F. Orbanić, M. Novak, Z. Glumac, A. McCollam, L. Tang, and I. Kokanović, Quantum oscillations of the magnetic torque in the nodal-line Dirac semimetal ZrSiS, Phys. Rev. B **103**, 045122 (2021).

[21] S. Pezzini, M. Van Delft, L. Schoop, B. Lotsch, A. Carrington, M. Katsnelson, N. E. Hussey, and S. Wiedmann, Unconventional mass enhancement around the Dirac nodal loop in ZrSiS, Nat. Phys. **14**, 178 (2018).

[22] Y. Yang, H. Xing, G. Tang, C. Hua, C. Yao, X. Yan, Y. Lu, J. Hu, Z. Mao, and Y. Liu, Anisotropic Berry phase in the Dirac nodal-line semimetal ZrSiS: The effect of spin-orbit coupling, Phys. Rev. B **103**, 125160 (2021).

[23] M. Matusiak, J. Cooper, and D. Kaczorowski, Thermoelectric quantum oscillations in ZrSiS, Nat. Commun. **8**, 15219 (2017).

[24] J. A. Voerman, L. Mulder, J. C. de Boer, Y. Huang, L. M. Schoop, C. Li, and A. Brinkman, Origin of the butterfly magnetoresistance in ZrSiS, Phys. Rev. Mater. **3**, 084203 (2019).

[25] D. Miertschin, T. Nguyen, S. R. Bhandari, K. Shtefiienko, C. Phillips, B. A. Magar, R. Sankar, D. E. Graf, and K. Shrestha, Anisotropic quantum transport in ZrSiS probed by high-field torque magnetometry, Phys. Rev. B **110**, 085140 (2024).

[26] B. Lorenz and C. Chu, High pressure effects on superconductivity, in *Frontiers in Superconducting Materials*, edited by A. V. Narlikar (Springer, Berlin, Heidelberg, 2005), pp. 459–497.

[27] M. Xu, Y. Li, and Y. Ma, Materials by design at high pressures, Chem. Sci. **13**, 329 (2022).

[28] K. Shtefiienko, C. Phillips, M. J. Stitz, G. Pokharel, S. D. Wilson, D. E. Graf, and K. Shrestha, Pressure effects on the Fermi surface of Ti-doped CsV_3Sb_5, Phys. Rev. B **111**, 235135 (2025).

[29] A. Dewaele and L. Nataf, Magnetic phase diagram of iron at high pressure and temperature, Phys. Rev. B **106**, 014104 (2022).

[30] I. Levatić, P. Popčević, V. Šurija, A. Kruchkov, H. Berger, A. Magrez, J. S. White, H. M. Rønnow, and I. Živković, Dramatic pressure-driven enhancement of bulk skyrmion stability, Sci. Rep. **6**, 21347 (2016).

[31] L. Deng, H.-C. Wu, A. P. Litvinchuk, N. F. Yuan, J.-J. Lee, R. Dahal, H. Berger, H.-D. Yang, and C.-W. Chu, Room-temperature skyrmion phase in bulk Cu_2oSeO_3 under high pressures, Proc. Natl. Acad. Sci. USA **117**, 8783 (2020).

[32] H. Takahashi, A. Sugimoto, Y. Nambu, T. Yamauchi, Y. Hirata, T. Kawakami, M. Avdeev, K. Matsubayashi, F. Du, C. Kawashima, *et al.*, Pressure-induced superconductivity in the iron-based ladder material $BaFe_2S_3$, Nat. Mater. **14**, 1008 (2015).

[33] J. Zhang, S. Zhang, H. Weng, W. Zhang, L. Yang, Q. Liu, S. Feng, X. Wang, R. Yu, L. Cao, *et al.*, Pressure-induced superconductivity in topological parent compound Bi_2Te_3, Proc. Natl. Acad. Sci. USA **108**, 24 (2011).

[34] K. Shrestha, L. Deng, K. Zhao, B. Jawdat, B. Lv, B. Lorenz, and C. Chu, Doping dependence and high-pressure studies on $Eu_xCa_{1-x}Fe_2As_2 (0 \leqslant x \leqslant 1)$, Supercond. Sci. Technol. **33**, 095010 (2020).

[35] A. Ohmura, Y. Higuchi, T. Ochiai, M. Kanou, F. Ishikawa, S. Nakano, A. Nakayama, Y. Yamada, and T. Sasagawa, Pressure-induced topological phase transition in the polar semiconductor BiTeBr, Phys. Rev. B **95**, 125203 (2017).

[36] X. Xi, C. Ma, Z. Liu, Z. Chen, W. Ku, H. Berger, C. Martin, D. B. Tanner, and G. L. Carr, Signatures of a pressure-induced topological quantum phase transition in BiTeI, Phys. Rev. Lett. **111**, 155701 (2013).

[37] W.-T. Guo, L. Huang, Y. Yang, Z. Huang, and J.-M. Zhang, Pressure-induced topological quantum phase transition in the magnetic topological insulator $MnBi_2Te_4$, New J. Phys. **23**, 083030 (2021).

[38] P. Barone, T. Rauch, D. Di Sante, J. Henk, I. Mertig, and S. Picozzi, Pressure-induced topological phase transitions in rocksalt chalcogenides, Phys. Rev. B **88**, 045207 (2013).

[39] C. Zhang, J. Sun, F. Liu, A. Narayan, N. Li, X. Yuan, Y. Liu, J. Dai, Y. Long, Y. Uwatoko, *et al.*, Evidence for pressure-induced node-pair annihilation in Cd_3As_2, Phys. Rev. B **96**, 155205 (2017).

[40] J. L. Zhang, C. Y. Guo, X. D. Zhu, L. Ma, G. L. Zheng, Y. Q. Wang, L. Pi, Y. Chen, H. Q. Yuan, and M. L. Tian, Disruption of the accidental Dirac semimetal state in $ZrTe_5$ under hydrostatic pressure, Phys. Rev. Lett. **118**, 206601 (2017).

[41] R. Singha, S. Samanta, S. Chatterjee, A. Pariari, D. Majumdar, B. Satpati, L. Wang, A. Singha, and P. Mandal, Probing lattice dynamics and electron-phonon coupling in the topological nodal-line semimetal ZrSiS, Phys. Rev. B **97**, 094112 (2018).

[42] L. Aggarwal, C. K. Singh, M. Aslam, R. Singha, A. Pariari, S. Gayen, M. Kabir, P. Mandal, and G. Sheet, Tip-induced superconductivity coexisting with preserved topological properties in line-nodal semimetal ZrSiS, J. Phys.: Condens. Matter **31**, 485707 (2019).

[43] C. C. Gu, J. Hu, X. L. Chen, Z. P. Guo, B. T. Fu, Y. H. Zhou, C. An, Y. Zhou, R. R. Zhang, C. Y. Xi, *et al.*, Experimental evidence of crystal symmetry protection for the topological nodal line semimetal state in ZrSiS, Phys. Rev. B **100**, 205124 (2019).

[44] D. VanGennep, T. A. Paul, C. W. Yerger, S. T. Weir, Y. K. Vohra, and J. J. Hamlin, Possible pressure-induced topological quantum phase transition in the nodal line semimetal ZrSiS, Phys. Rev. B **99**, 085204 (2019).

[45] J. P. Lorenz, J. F. Linnartz, A. Kool, M. R. Van Delft, W. Guo, I. Aguilera, R. Singha, L. M. Schoop, N. E. Hussey, S. Wiedmann, and A. de Visser, Uniaxial strain effects on the Fermi surface and quantum mobility of the Dirac nodal-line semimetal ZrSiS, Phys. Rev. B **109**, 235114 (2024).

[46] P. Blaha, K. Schwarz, G. K. Madsen, D. Kvasnicka, J. Luitz, *et al.*, Wien2k, An augmented plane wave+ local orbitals program for calculating crystal properties (2001), http://www.wien2k.at/reg_user/textbooks/usersguide.pdf?_gl=1∗1t25jaa∗_gcl_au∗MTk4NjA3NjQxNy4xNzcxMDE5NTQx∗_ga∗MTQ1NzY1MzI3OS4xNzYzMjM5MDg1∗_ga_ZS5V2B2DR1∗czE3NzYxOTI0OTYkbzE4OSRnMSR0MTc3NjE5NDEwNCRqNDckbDAkaDg1OTQzMzgwMA.

[47] J. P. Perdew, K. Burke, and M. Ernzerhof, Generalized gradient approximation made simple, Phys. Rev. Lett. **77**, 3865 (1996).

[48] K. Koepernik and H. Eschrig, Full-potential nonorthogonal local-orbital minimum-basis band-structure scheme, Phys. Rev. B **59**, 1743 (1999).

[49] I. Opahle, K. Koepernik, and H. Eschrig, Full-potential band-structure calculation of iron pyrite, Phys. Rev. B **60**, 14035 (1999).

[50] P. Giannozzi, S. Baroni, N. Bonini, M. Calandra, R. Car, C. Cavazzoni, D. Ceresoli, G. L. Chiarotti, M. Cococcioni, I. Dabo, *et al.*, QUANTUM ESPRESSO: a modular and open-source software project for quantumsimulations of materials, J. Phys.: Condens. Matter **21**, 395502 (2009).

[51] G. Kresse and J. Furthmüller, Efficient iterative schemes for *ab initio* total-energy calculations using a plane-wave basis set, Phys. Rev. B **54**, 11169 (1996).

[52] A. Togo and I. Tanaka, First principles phonon calculations in materials science, Scr. Mater. **108**, 1 (2015).

[53] K. Shtefiienko, C. Phillips, S. Mozaffari, R. P. Madhogaria, W. R. Meier, D. G. Mandrus, D. E. Graf, and K. Shrestha, Electronic structure of YV_6Sn_6 probed by de Haas–van Alphen oscillations and density functional theory, APL Quantum **2**, 016118 (2025).

[54] C. Phillips, K. Shtefiienko, S. Mozaffari, R. P. Madhogaria, W. R. Meier, A. F. Savvidou, B. W. Casas, L. Balicas, D. G. Mandrus, D. E. Graf, *et al.*, Electrical transport and torque magnetometry studies of the kagome compound LuV_6Sn_6 under high magnetic fields, Phys. Rev. B **111**, 155136 (2025).

[55] D. Shoenberg, *Magnetic Oscillations in Metals* (Cambridge University Press, 2009).

[56] K. Shtefiienko, C. Phillips, B. R. Ortiz, D. E. Graf, and K. Shrestha, Electronic structure of the kagome metal $YbTi_3Bi_4$ studied using torque magnetometry, Phys. Rev. B **111**, 035145 (2025).

[57] K. Shrestha, M. Shi, T. Nguyen, D. Miertschin, K. Fan, L. Deng, D. E. Graf, X. Chen, and C.-W. Chu, Fermi surface mapping of the kagome superconductor RbV_3Sb_5 using de Haas-van Alphen oscillations, Phys. Rev. B **107**, 075120 (2023).

[58] K. Shrestha, B. Regmi, G. Pokharel, S.-G. Kim, S. D. Wilson, D. E. Graf, B. A. Magar, C. Phillips, and T. Nguyen, Electronic properties of kagome metal ScV_6Sn_6 using high-field torque magnetometry, Phys. Rev. B **108**, 245119 (2023).

[59] K. Shrestha, V. Marinova, D. Graf, B. Lorenz, and C. W. Chu, Quantum oscillations in metallic Sb_2Te_2Se topological insulator, Phys. Rev. B **95**, 075102 (2017).

[60] S. R. Bhandari, M. Zeeshan, V. Gusain, K. Shrestha, and D. Rai, First-principles study of the electronic structure, $\mathbb{Z}_2$ invariant, and quantum oscillation in the kagome material CsV_3Sb_5, APL Quantum **1**, 046118 (2024).

[61] D. Gurung, K. Shrestha, S. R. Bhandari, S. Brahimi, S. Lounis, and D. P. Rai, Electronic properties of Kagome metal YbV_3Sb_4: A first-principles study, Phys. Rev. Mater. (2026), doi: 10.1103/kk79-9vkx.

[62] X. Jin, Q. Zhang, D. Li, Z. Cheng, J. Wang, X. Lv, X. Zhou, R. Wang, X. Ding, P. Yu, *et al.*, Anharmonicity-driven avoided phonon crossing and anomalous thermal transport in the nodal-line semimetal ZrSiS, Phys. Rev. B **112**, 184311 (2025).

[63] W. Zhou, H. Gao, J. Zhang, R. Fang, H. Song, T. Hu, A. Stroppa, L. Li, X. Wang, S. Ruan, *et al.*, Lattice dynamics of Dirac node-line semimetal ZrSiS, Phys. Rev. B **96**, 064103 (2017).